

Thickness-dependent physical and nanomechanical properties of $\text{Al}_x\text{Ga}_{1-x}\text{N}$ thin films

N. Boughrara^{a,*}, Z. Benzarti^{a,*}, A. Khalfallah^{b,c,d}, J.C. Oliveira^b, M. Evaristo^b, A. Cavaleiro^b

^a Laboratory of Multifunctional Materials and Applications (LaMMA), Department of Physics, Faculty of Sciences of Sfax, University of Sfax, Soukka Road km 3.5, B.P. 1171, 3000, Sfax, Tunisia

^b University of Coimbra, CEMMPRE - Centre for Mechanical Engineering Materials and Processes, Department of Mechanical Engineering, Rua Luís Reis Santos, Coimbra, 3030-788, Portugal

^c Laboratoire de Genie Mécanique, Ecole Nationale d'Ingénieurs de Monastir, Université de Monastir, Av. Ibn El-Jazzar, 5019, Monastir, Tunisia

^d DGM, Institut Supérieur des Sciences Appliquées et de Technologie de Sousse, Université de Sousse, Cité Ibn Khaldoun, 4003, Sousse, Tunisia

ARTICLE INFO

Keywords:

$\text{Al}_x\text{Ga}_{1-x}\text{N}$ film Thickness
Surface morphology
Defects
Stress relaxation
Nanoindentation
Pop-in

ABSTRACT

A set of undoped $\text{Al}_x\text{Ga}_{1-x}\text{N}$ epilayers with different thicknesses were grown on (0001) sapphire substrates using metal-organic chemical vapor deposition (MOCVD) technique, using the same gas-phase composition of trimethylaluminum (TMAl) and trimethylgallium (TMGa). Giving that the first growth stage is crucial for the successful fabrication of $\text{Al}_x\text{Ga}_{1-x}\text{N}$ epilayers; thus, SiN nano-mask, as an alternative method to nanoimprint lithography (NIL) which is used for patterning substrates, was deposited on sapphire substrate. Indeed, SiN treatment initiates the three-dimensional (3D) growth mode to efficiently decrease the threading dislocation density. It was found that depending on the film surface coalescence degree, the physical and nanomechanical properties are thoroughly dependent. As the non-coalescent surface is present, the porosity effects are dominant. As soon as the film thickness attains the surface coalescence, the Al incorporation is enhanced and conveyed with it point defects. Despite the decrease of the threading dislocations along with the film thickness evolution, it was observed that the physical properties are slightly decreased and the nanomechanical properties are improved. This is likely related to point defect interaction with nucleated dislocations. Moreover, the defects did not severally affect the plastic deformation capacity (ductility) of $\text{Al}_x\text{Ga}_{1-x}\text{N}$ films, where high indentation force was applied and no failure was revealed. Therefore, the balance between $\text{Al}_x\text{Ga}_{1-x}\text{N}$ physical and nanomechanical performances devotes to manufacture a wider range of efficient UV devices.

1. Introduction

Nowadays, III-nitride semiconductors (AlN, GaN, InN) and their compounds are considered as ones of the most important groups for optoelectronic applications such as UV and blue light-emitting diodes (LEDs) [1–3], UV and blue laser diodes [4–6], UV sensors [7] and UV photodetectors [8,9]. Among these nitrides, $\text{Al}_x\text{Ga}_{1-x}\text{N}$ devices have been widely used for different applications owing to its direct bandgap ranging from 3.4 eV to 6.2 eV depending on Al content [10] and to its high power and high electron mobility transistors [11]. The growth of $\text{Al}_x\text{Ga}_{1-x}\text{N}$ layers with metal-organic chemical vapor deposition (MOCVD) technique is one of the most successful methods used in III-nitride thin film growth process [12].

Several studies have reported the dependence of the physical

properties of $\text{Al}_x\text{Ga}_{1-x}\text{N}$ films on layer thickness [13–15], and Al composition [16,17] effects. Pasayet et al. [14] observed an enhancement in Al incorporation when $\text{Al}_x\text{Ga}_{1-x}\text{N}$ film thickness increases. On the other hand, the investigation of nanomechanical properties of $\text{Al}_x\text{Ga}_{1-x}\text{N}$ films obtained using nanoindentation technique have attracted substantial attention of several researchers [18,19]. Indeed, the nanomechanical characteristics of $\text{Al}_x\text{Ga}_{1-x}\text{N}$ materials are also key factors for its successful application. For instance, the contact loading during fabrication or packaging can seriously damage the devices' performance. Nanoindentation is a fundamental method to determine the hardness and elastic modulus of thin films. Commonly, elastic/plastic behaviors are inherent in the loading-unloading curves. The analysis of loading curves reveals in certain conditions an important phenomenon so-called “pop-in” event. The first pop-in event reveals the onset of

* Corresponding author.

E-mail address: zohra.benzarti@fss.usf.tn (Z. Benzarti).

plasticity [20–22]. Based on classical dislocation theory, pop-in is attributed to the homogenous dislocation nucleation [20,23,24]. Similar events are revealed in several materials such as MgO [25], single-crystal silicon [26], InP and GaAs [27].

For $\text{Al}_x\text{Ga}_{1-x}\text{N}$ based devices, it remains huge efforts to improve their performance such as UV LEDs light output power. The principal responsible factor in the low performance of LEDs is the heteroepitaxy of $\text{Al}_x\text{Ga}_{1-x}\text{N}$ on sapphire, which is the commonly used substrate. In other words, the major issue of the $\text{Al}_x\text{Ga}_{1-x}\text{N}$ growth on sapphire substrate is the strong lattice mismatch and the thermal expansion coefficient between them, which involve high biaxial strains [14] and density defects [13]. These latter, trap carries, act as non-radiative recombination centers, and thus impact the optoelectrical properties of grown layers. To overcome these drawbacks, it was proposed to deposit on sapphire, GaN or AlN buffer layers at low-temperature [28,29]. The epitaxial lateral overgrowth (ELO) was also an alternative method [5,30]. This ELO technology needs more complicated and expensive ex-situ steps.

While the above-mentioned techniques demonstrated efficiency to reduce the effect of the threading dislocations and therefore increase the internal quantum efficiency, the SiN treatment emerges as a helpful technique used for reducing the costs and improve throughput fabrication of nitride semiconductors. It was shown that SiN treatment was proved as reliable method to elaborate high crystal $\text{Al}_x\text{Ga}_{1-x}\text{N}$ quality [31]. The principle of this method is based on the deposition of random *in-situ* nano-mask on sapphire substrate to instigate the 3D growth mode. SiN treatment contribute to annihilate almost the threading dislocations by image force from the void sidewalls before coalescence [12,32]. Indeed, the high quality $\text{Al}_x\text{Ga}_{1-x}\text{N}$ layer is also dependent on the growth parameters, such as growth temperature, III/V ratio, template polarity and eventually the film thickness. Therefore, the operator can tune these growth parameters along with the SiN treatment to tailor the $\text{Al}_x\text{Ga}_{1-x}\text{N}$ properties' layer with the desired UV LEDs technical specifications.

Moreover, the nanoimprint lithography technique, which was proposed in the middle of the nineties by Chou et al. [33] emerges as another approach used to reduce threading dislocations and defects by introducing patterned sapphire substrates to the nanoscale [34]. This nanoscale fabrication process is featured with the potential for low cost and high efficiency. For instance, to improve nitride LEDs performances using patterned sapphire substrates, two possible practices are utilized. First, the patterned sapphire substrates reduce considerably the lattice mismatch between the substrate and the nitride layer [35]. Second, the patterned interface reduces the reflected light, which is typically absorbed by the electrode, by scattering the emitted light and then increase light extraction efficiency [36]. On the other hand, the patterned electrode surfaces of LEDs could be another efficient approach to reduce the light scattering losses in other interface with LEDs structure [37]. Nanoimprint lithography was also used to transfer patterned designs on LEDs' electrode surfaces to improve output power performances [38]. However, the commonly used approach to texture electrode surfaces is the unpartnered etching practice. The conjunction of both patterned sapphire substrates and patterned electrode surfaces for LEDs is likely a prominent approach to highly increase their internal and external quantum efficiency as using photonic crystals on top of LEDs [39].

One may wonder on the potential efficiency of surface patterning with only one step using embossing or stamping process on the LEDs surface utilizing a hard mold/patterned die. This exciting and prospective approach is likely low cost and a good alternative to the conventional nanoimprint lithography. In such exciting outcomes, the high challenges are to determine the growth parameters which are the key factors that control the set of physical and nanomechanical properties to achieve the optimal LEDs performances. In other words, the target of the operator is the balance between the ductility and the stiffness of $\text{Al}_x\text{Ga}_{1-x}\text{N}$ layers along with acceptable low dislocation density to elaborate efficient UV LEDs.

To the best of our knowledge, the study of nanomechanical properties of $\text{Al}_x\text{Ga}_{1-x}\text{N}$ epilayers elaborated on sapphire substrates using SiN

nano-mask has been seldom reported. The selected samples were elaborated in the purpose to obtain the best $\text{Al}_x\text{Ga}_{1-x}\text{N}$ film nanomechanical properties suitable for the elaboration of high-performance UV LEDs for likely a large-scale devices' manufacturing. It was shown that, as the $\text{Al}_x\text{Ga}_{1-x}\text{N}$ epilayer thickness increases, the resulting surface coalescence degree dictates the physical and nanomechanical properties.

2. Experimental details

Undoped $\text{Al}_x\text{Ga}_{1-x}\text{N}$ films were grown at 1120 °C on (0001) sapphire substrate by atmospheric metal-organic chemical vapor deposition (MOCVD) using trimethylaluminum (TMAl), trimethylgallium (TMGa) and ammonia (NH_3) as precursors for Al, Ga and N, respectively. The carrier gases, used during the growth process, were a mixture of hydrogen (H_2) and nitrogen (N_2). After a substrate nitridation step at 1120 °C in NH_3 (3 slm) + N_2 (2 slm) + H_2 (2 slm) ambient for 10 mn, the SiN treatment was carried out by introducing 10 sccm of silane (SiH_4) into the reactor at the same temperature for 120 s. This leads to a partial covering of the sapphire substrate by a random SiN nano-mask, which facilitates the formation of a nano-selective area growth of $\text{Al}_x\text{Ga}_{1-x}\text{N}$. Then, the temperature was dropped to 600 °C for the deposition of a 30 nm thick GaN buffer/nucleation layer. After a temperature ramp from 600 °C to 1120 °C, $\text{Al}_x\text{Ga}_{1-x}\text{N}$ epilayer was finally grown with 10 sccm of TMGa and 6 sccm of TMAl. More details of growth process conditions were reported in Refs. [17,40,41]. Four $\text{Al}_x\text{Ga}_{1-x}\text{N}$ samples were elaborated at different growth stages with the same gas-phase compositions of TMAl and TMGa. These thin layers labelled S_0 , S_1 , S_2 and S_3 , have the thickness of 210 nm, 400 nm, 650 nm and 1200 nm, respectively. The $\text{Al}_x\text{Ga}_{1-x}\text{N}$ layer thickness was in-situ monitored by laser reflectometry set-up [17]. In ex-situ control, the layer thickness was determined by scanning electron microscope (SEM) cross-section measurements.

Thereafter, the variation of the Al solid content (x) was obtained for $\text{Al}_x\text{Ga}_{1-x}\text{N}$ S_3 sample using secondary ion mass spectrometry (SIMS) analysis by means of EVANS EAST via Cesium ion bombardment.

Furthermore, dislocation density is determined from the high-resolution X-ray diffraction (HRXRD). The electron mobility and the refractive index of $\text{Al}_x\text{Ga}_{1-x}\text{N}$ samples are determined from the Hall-effect measurements (the standard Van der Pauw configuration) and from spectroscopic ellipsometry (the automatic ellipsometer SOPRA-GES5), respectively. In order to evaluate the effect of Al incorporation, a comparative study was established between the physical and nanomechanical properties of the $\text{Al}_x\text{Ga}_{1-x}\text{N}$ layer (S_3) and GaN film which were elaborated at similar growth conditions. Both samples have the same thickness (1200 nm) and they achieved the bidimensional (2D) growth mode.

The nanomechanical properties of $\text{Al}_x\text{Ga}_{1-x}\text{N}$ thin films deposited on sapphire substrate were tested using a nanoindentation instrument (NanoTest NT1, NanoMaterials, Ltd) equipped with a pyramid-shaped Berkovich-type diamond indenter tip of a 700 nm curvature tip radius and a 65.3° semi-apex angle. Prior to indentation tests, the indenter facility was carefully calibrated using Fused silica. It is worth to mention that nanoindentation measurements for the thinnest S_0 sample, are not considered, because the indenter tip exceeds 30% of the film thickness for the used maximal forces in this study. The indentation depths should be usually set below a threshold depth percentage relative to the film thickness to avoid the substrate effect on measured properties. For each sample, 16 indentation tests were performed at room temperature providing load-displacement (P - h) curves which reflect the nanomechanical behavior of volume material deformed underneath the indenter tip. These indentations were sufficiently spaced of about 30 μm to avoid any interactions and the dwell time was taken equal to 30 s at the maximum load. They were performed at maximum loads of 4 mN with a loading rate of 0.15 mN/s. Hardness and Young's modulus were calculated from the loading-unloading curves using the Oliver and Pharr method [42]. To further check the aspects of nanoimprints marked on the samples' surfaces and whether cracks were occurred or not, a high

indentation load as high as 200 mN was utilized. The scanning electron microscope (SEM) was used in the examination of imprints and the surface morphology of these four epilayers. Furthermore, nano-indentation tests were performed on fully coalesced $\text{Al}_x\text{Ga}_{1-x}\text{N}$ and GaN layers of 1200 nm-thick at maximal load of 10 mN to probe the effect of Al incorporation on nanomechanical response of thickest sample (S3) for comparison purpose.

3. Results and discussion

3.1. Analysis of physical properties

Fig. 1 presents SEM images of $\text{Al}_x\text{Ga}_{1-x}\text{N}$ epilayers. S_0 , S_1 , S_2 , and S_3 samples were elaborated at identical growth conditions. They are featured by their thickness value difference. During the initial growth stage, the surface morphology exhibits a high pore density and a perceived random pervasion of pores on the sample surface (Fig. 1a), indicating the 3D growth mode. The surface porosity is gradually reduced with the increase of $\text{Al}_x\text{Ga}_{1-x}\text{N}$ layer thickness, as surface coalescence is augmenting. This indicates that the 2D growth mode is taking place and leading gradually to smoother sample surface, as shown in Fig. 1d. The dwindle of pore density is basically attributed to the coalescence of large islands formed during the growth process of the $\text{Al}_x\text{Ga}_{1-x}\text{N}$ layer, as the film thickness increases. Consequently, the film thickness influences the surface morphology of $\text{Al}_x\text{Ga}_{1-x}\text{N}$ layers, as the surface is featured by discontinuous islands (3D growth mode) at the first growth stage and evolves to a continuous surface (2D growth mode) for thicker films. Similar growth mode was observed in GaN epilayers, where SiN nano-mask was deposited on sapphire substrate. This nano-mask was shown the responsible for the appearance of large islands at the first stages of GaN growth, followed by a coalescence process [43].

In order to assess the structural characteristics of $\text{Al}_x\text{Ga}_{1-x}\text{N}$ samples, high-resolution X-ray diffraction (HRXRD) measurements were performed. The full width at half maximum (FWHM) of their X-ray rocking curves is also commonly evaluated. Both symmetric (0002) and asymmetric (10 $\bar{1}$ 5) rocking curves of $\text{Al}_x\text{Ga}_{1-x}\text{N}$ samples S_0 , S_1 , S_2 , and S_3 are shown in Fig. 2. Table 1 lists FWHM results of the rocking curves of (0002) and (10 $\bar{1}$ 5) planes. It is clearly seen that the measured FWHM of (0002) and (10 $\bar{1}$ 5) reflections are highly reduced along with the increase of the $\text{Al}_x\text{Ga}_{1-x}\text{N}$ layer thickness. In the 2D growth mode, FWHM values are 343 arcsec and 362 arcsec for (0002) and (10 $\bar{1}$ 5) reflections, respectively. Thus, high crystalline quality is obtained for S_3 sample due to its lower FWHM compared to other samples.

To estimate the dislocation density of $\text{Al}_x\text{Ga}_{1-x}\text{N}$ films, the following equations are used [44,45]:

$$D_{\text{screw}} = \frac{(\text{FWHM})_{(0002)}^2}{4.35b_{\text{screw}}^2} \quad (1)$$

$$D_{\text{edge}} = \frac{(\text{FWHM})_{(10\bar{1}5)}^2}{4.35b_{\text{edge}}^2} \quad (2)$$

where b is the Burgers vector length ($b_{\text{edge}} = 0.3189$ nm and $b_{\text{screw}} = 0.5815$ nm). D_{screw} and D_{edge} correspond to the screw and edge dislocation densities, respectively.

As the film thickness increases, screw and edge dislocation densities decrease and thus, the total dislocation density decreases. Fig. 3 displays the total dislocation density evolution along with the film thickness of $\text{Al}_x\text{Ga}_{1-x}\text{N}$ layers. One can see that the dislocation density is $7.94 \times 10^9 \text{ cm}^{-2}$ at the initial stage of the growth process (S_0 sample) and it reaches $8.83 \times 10^8 \text{ cm}^{-2}$ for the thicker $\text{Al}_x\text{Ga}_{1-x}\text{N}$ film (S_3 sample). This

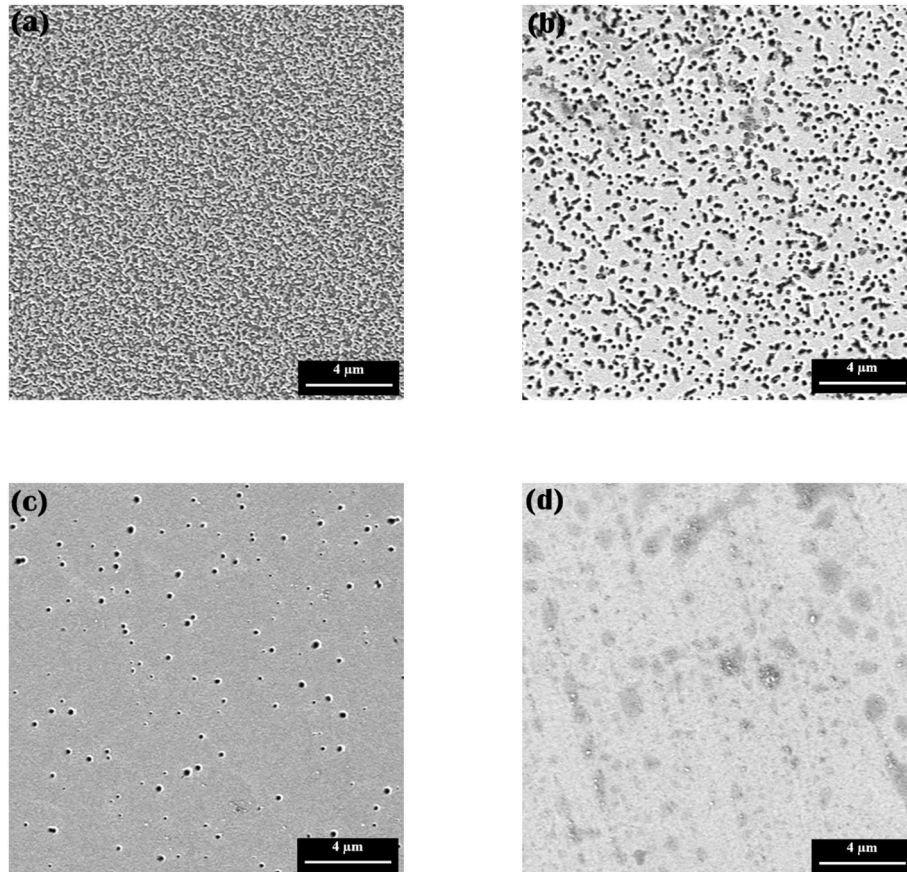


Fig. 1. SEM images of $\text{Al}_x\text{Ga}_{1-x}\text{N}$ thin films: (a) S_0 , (b) S_1 , (c) S_2 and (d) S_3 .

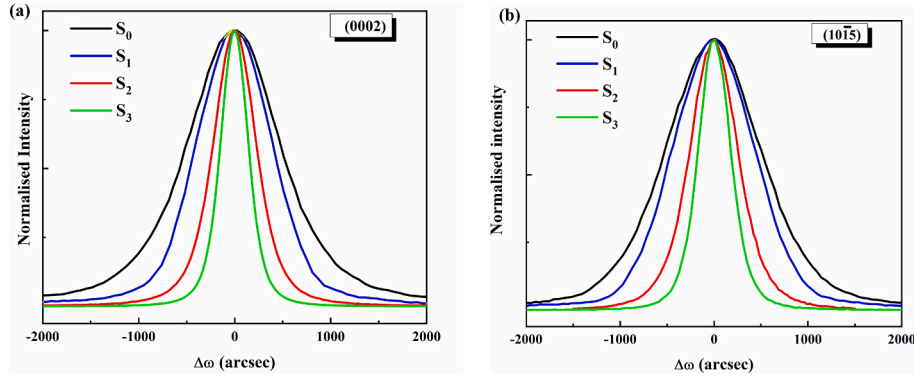


Fig. 2. HRXRD rocking curves of: (a) symmetric (0002) and (b) asymmetric (10 $\bar{1}$ 5) reflections of Al_xGa_{1-x}N samples (S₀, S₁, S₂ and S₃).

Table 1

FWHM of symmetric (0002) and asymmetric (10 $\bar{1}$ 5) rocking curves and dislocation densities for different Al_xGa_{1-x}N samples (S₀, S₁, S₂ and S₃).

Al _x Ga _{1-x} N Sample	Thickness (nm)	(0002) FWHM (arcsec)	D _{screw} (cm ⁻²)	(10 $\bar{1}$ 5) FWHM (arcsec)	D _{edge} (cm ⁻²)
S ₀	210	1124	2.02x10 ⁹	1056	5.92x10 ⁹
S ₁	400	863	1.19x10 ⁹	880	4.11x10 ⁹
S ₂	650	529	4.47x10 ⁸	525	1.46x10 ⁹
S ₃	1200	343	1.88x10 ⁸	362	6.95x10 ⁸

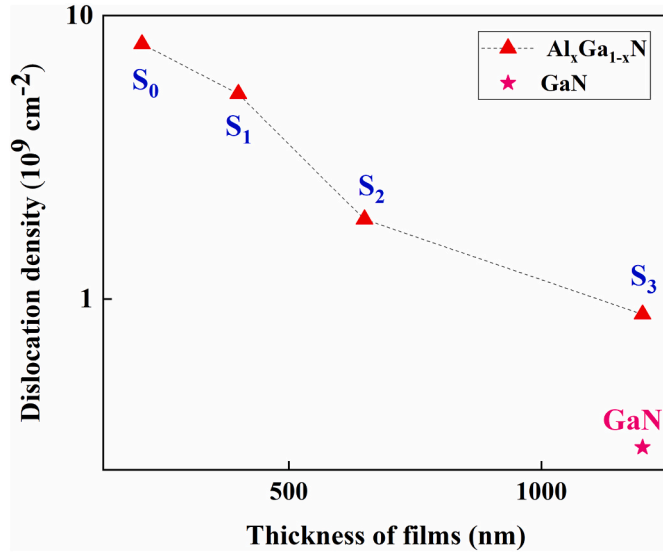


Fig. 3. The measured dislocation density deduced from FWHM rocking curves, obtained for different Al_xGa_{1-x}N samples (S₀, S₁, S₂ and S₃). Solid star represents dislocation density of GaN sample elaborated at the same growth conditions as S₃ sample.

reduction of dislocation density reveals the improvement of the crystalline quality. This result is in agreement with Refs [31,46]. The formation and propagation of high dislocation density take place at the first stage of the Al_xGa_{1-x}N growth process. In fact, a high dislocation density is noticeably marked near the sapphire interface, favored by the lattice mismatch. In addition, the threading dislocations are generated and emerged during the Al_xGa_{1-x}N growth process, once the coalescence of adjacent islands is achieved [47]. Al_xGa_{1-x}N large islands, obtained by the SiN nano-mask, are found to be truncated shapes at the threshold of the 2D growth mode [48,49]. The threading dislocations may be blocked at the truncated facets and embedded into the sample, as long as the

thickness increases. Consequently, the dislocation density is dropped. One can conclude that dislocation density decreases with increasing the Al_xGa_{1-x}N layer thickness, which improved crystalline quality of the layer through the smoothing process, as observed in SEM images (Fig. 1).

Moreover, the dislocation density of the thicker Al_xGa_{1-x}N sample is compared to those of GaN sample in order to highlight the effect of Al atoms incorporation. Fig. 3 indicates that the dislocation density found for S₃ sample ($\sim 9 \times 10^8$ cm⁻²) is higher than that for GaN sample. It is interesting to notice that the incorporation of Al atoms introduces point defects which are responsible for the distinguish defect density of Al_xGa_{1-x}N film compared to GaN one.

Fig. 4 shows the evolution of Ga and Al atoms versus the depth throughout the thickness layer of S₃ sample. The deduced Al solid content (x) profile through the Al_xGa_{1-x}N sample thickness is recorded. SIMS results show that the Al solid composition increases progressively along with the Al_xGa_{1-x}N layer thickness increase, then it reaches a steady value of almost 7% while the layer surface coalescence.

Fig. 5 displays the stress values of Al_xGa_{1-x}N layers against the Al_xGa_{1-x}N thickness. Two distinct regions are revealed when the film thickness increases.

The stress (σ) is expressed by the following equation [50]:

$$\sigma = \frac{E}{1 - \nu} \epsilon_{//} \quad (3)$$

Where E corresponds to Young's modulus of each sample, ν is the Poisson coefficient, and $\epsilon_{//}$ is the compressive strain. It is important to highlight that all Al_xGa_{1-x}N samples grown on SiN treated sapphire

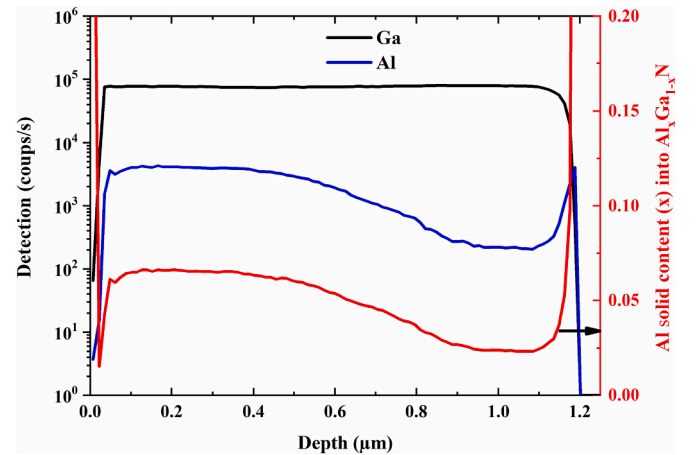


Fig. 4. SIMS profile of Al (solid blue line) and Ga (solid black line) atoms obtained for the thicker Al_xGa_{1-x}N layer (S₃ sample). The solid red line represents the variation of the Al solid content (x) into Al_xGa_{1-x}N layer.

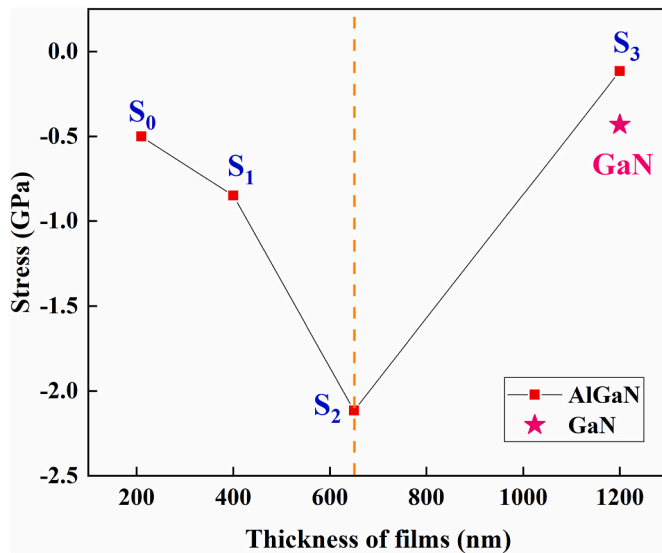


Fig. 5. Stress evolution against the $\text{Al}_x\text{Ga}_{1-x}\text{N}$ layer thickness. GaN layer stress was plotted for comparison purpose. Dashed line marks the transition from 3D to 2D growth mode.

substrate are under compressive strain, as shown in Fig. 5. The analysis of the stress evolution along with $\text{Al}_x\text{Ga}_{1-x}\text{N}$ thickness shows that firstly, the absolute value of stress increases with the increase of $\text{Al}_x\text{Ga}_{1-x}\text{N}$ film thickness until it attains 650 nm (S_2 sample). Secondly, with further increase of $\text{Al}_x\text{Ga}_{1-x}\text{N}$ film thickness up to 1200 nm, a significant decrease of absolute stress is noticed. This indicates a stress relaxation, once the coalescence process is achieved. Indeed, during the early growth stages, the relative high strain value is attained at the beginning of islands formation, as shown for S_0 sample. In this growth stage, competitive adsorption of Al and Ga atoms is occurred [51]. The incorporation of Ga atoms into the layer surface inhibits the Al atoms incorporation [16] and contributes to islands formation besides to their size increase. Despite its less mobility compared to Ga atoms, Al atoms promote the enlargement of these islands as long as the growth process continues. Then, the stress increases with the increase of the film thickness up to the transition of 3D-2D growth mode. Thereafter, the stress decreases until the thickness layer reaches its maximum value (1200 nm), as shown for S_3 sample. This is directly correlated to the coalescence of large islands process followed by stress relaxation at the high Al content as shown in Fig. 4. Previous studies attributed this stress relaxation to the release of pulling effect in $\text{Al}_x\text{Ga}_{1-x}\text{N}$ samples [52,53]. At the beginning of the growth process, most of Al atoms are pulled out of the layers, which are under compressive strain induced by the lattice mismatch between $\text{Al}_x\text{Ga}_{1-x}\text{N}$ and sapphire substrate [54]. In our case, once the coalescence process of $\text{Al}_x\text{Ga}_{1-x}\text{N}$ layer is achieved, a reduction of stresses along with high Al atoms incorporation is obtained. It is interesting to note that the GaN stress absolute value is higher than that for $\text{Al}_x\text{Ga}_{1-x}\text{N}$ sample (S_3), as displayed in Fig. 5. One can assume that Al atoms are generally the main source of this difference of stress relaxation between these two samples (about 1200 nm). Several studies demonstrated the existence of different mechanisms responsible for this stress relaxation within $\text{Al}_x\text{Ga}_{1-x}\text{N}$ layers, such as relaxation with the generation of cracks [55], relaxation by the propagation of dislocations [56], or by the propagation of point defects [57]. For $\text{Al}_x\text{Ga}_{1-x}\text{N}$ films, HRXRD measurements show a sharp decline in dislocation density with the increase of film thickness. Moreover, SEM results demonstrated a crack-free surface (Fig. 1d). This leads to conclude that the dominant process of stress relaxation is probably associated with the generation of point defects. One can deduce that Al atoms could be the major primary origin of these defects within thicker films.

Fig. 6 depicts the refractive index against $\text{Al}_x\text{Ga}_{1-x}\text{N}$ layer thickness

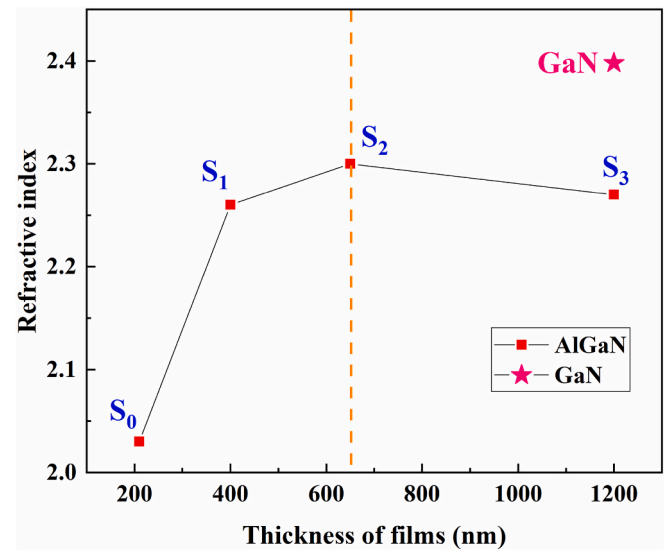


Fig. 6. Refractive index evolution against the $\text{Al}_x\text{Ga}_{1-x}\text{N}$ thickness obtained for 600 nm wavelength. GaN layer refractive index was plotted for comparison purpose. Dashed line marks the transition from 3D to 2D growth mode.

that are deduced from ellipsometry measurements obtained for 600 nm wavelength. The refractive index increases gradually until it reaches 2.30 for S_2 sample (~650 nm), then it decreases to 2.27 for S_3 sample, for which the Al content is the highest. Firstly, the increase of the refractive index confirms that the porosity of the $\text{Al}_x\text{Ga}_{1-x}\text{N}$ films decreases until reaching the phase transition of 3D-2D growth mode. Note that the refractive index in this first domain is highly dependent on the void fraction in $\text{Al}_x\text{Ga}_{1-x}\text{N}$ films. Secondly, the density of pores decreases where it is expected to have higher refractive index value. But, the obtained refractive index of the thickest layer decreases. This is likely attributed to the Al content increase since the refractive index of AlN layer is lower than that of GaN layer [58]. Indeed, for samples thickness of 1200 nm, the refractive index of GaN layer (2.39) is higher than that of $\text{Al}_x\text{Ga}_{1-x}\text{N}$ layer (2.27). So, we can deduce that the refractive index evolution is dictated by the porosity for thinner $\text{Al}_x\text{Ga}_{1-x}\text{N}$ layers; however, for thicker $\text{Al}_x\text{Ga}_{1-x}\text{N}$ layers, it is dominated by Al incorporation effect.

Besides the optical characteristics, the effect of these defects on electrical properties of $\text{Al}_x\text{Ga}_{1-x}\text{N}$ films is studied using the Van der Pauw-Hall technique. The variation of the electron density and mobility against layer thickness is shown in Fig. 7. On one hand, as the thickness increases and the dislocation density decreases, the electron density decreases from $8.6 \times 10^{19} \text{ cm}^{-3}$ to $4.5 \times 10^{18} \text{ cm}^{-3}$. In fact, SiN nano-mask was deposited on sapphire substrate using MOCVD process to reduce the mismatch in the interface $\text{Al}_x\text{Ga}_{1-x}\text{N}$ /substrate. However, carbon, silicon and oxygen impurities are unintentionally incorporated. These impurities are resulting in the high electron density at the first growth stages. On the other hand, the electron mobility increases and then decreases after coalescence process. It is worth to note that the trend of the electron mobility along with the film thickness is similar to that of the refractive index.

It is shown that the electron mobility of $\text{Al}_x\text{Ga}_{1-x}\text{N}$ layers increases with film thickness increase until it reaches $55 \text{ cm}^2/\text{V.s}$ at 650 nm (S_2 sample). In contrast, it is found that the electron mobility decreases once the film thickness exceeds this value. It is about $31 \text{ cm}^2/\text{V.s}$ for S_3 sample. Regarding these findings that exhibit a systematic study of physical in relationship with nanomechanical properties along with the sample's thickness increase. It was shown a good correlation between the electrical properties and the growth modes dictated by SiN treatment on substrates of $\text{Al}_x\text{Ga}_{1-x}\text{N}$ samples. In fact, in the first stage of the growth process, a high dislocation density is accompanied by the

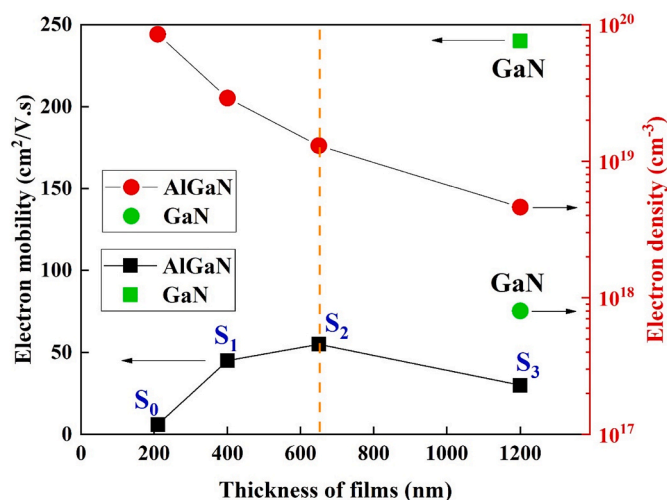


Fig. 7. Electron density (solid red circle) and mobility (solid black square) against the sample thickness of $\text{Al}_x\text{Ga}_{1-x}\text{N}$ layers. GaN layer electron density (solid green circle) and mobility (solid green square) were plotted for comparison purpose. Dashed line marks the transition from 3D to 2D growth mode.

initiation of islands formation near the $\text{Al}_x\text{Ga}_{1-x}\text{N}$ /sapphire interface. A high density of pores is disseminated in sample surface, which points out the low electron mobility. Moreover, an increase in the electron mobility is expected with the increase of $\text{Al}_x\text{Ga}_{1-x}\text{N}$ thickness up to the transition of 3D-2D growth mode (S_2 sample). At this step, the electron mobility reaches its maximum value whereas the dislocation density shows a progressive decline. This suggests that before reaching the 2D growth mode, the electron mobility depends on the void fraction in $\text{Al}_x\text{Ga}_{1-x}\text{N}$ films (3D surface morphology). Once the 2D growth mode process is achieved, a low dislocation density is evolved with high Al content, and further is followed by a drop in the electron mobility (S_3 sample). This behavior is likely interpreted by only Al atoms influence on electrical properties of S_3 sample. This is corroborated by ellipsometry measurements (Fig. 6). In order to confirm this statement, it is highly interesting to compare the electrical results obtained for GaN and $\text{Al}_x\text{Ga}_{1-x}\text{N}$ samples for which they complete their 2D growth mode (1200 nm). Obviously, the $\text{Al}_x\text{Ga}_{1-x}\text{N}$ sample (S_3) has 7% of Al content, whereas the second (GaN) is free Al atoms. On one hand, the electron density of GaN sample ($8.1 \times 10^{17} \text{ cm}^{-3}$) is lower than that of $\text{Al}_x\text{Ga}_{1-x}\text{N}$ sample ($4.5 \times 10^{18} \text{ cm}^{-3}$). On the other hand, the electron mobility shows higher value for GaN sample ($240 \text{ cm}^2/\text{V.s}$) than that for $\text{Al}_x\text{Ga}_{1-x}\text{N}$ sample ($31 \text{ cm}^2/\text{V.s}$). One can deduce that Al atoms are responsible for the reduction of electron mobility. This result is confirmed by Benzarti et al. [12,17]. They demonstrated that the transitional growth mode has occurred when the electron mobility increases for GaN layer and decreases for $\text{Al}_x\text{Ga}_{1-x}\text{N}$ layer.

Moreover, it was demonstrated that the main defect source that affects the electron mobility in $\text{Al}_x\text{Ga}_{1-x}\text{N}$ samples is the formation of Al vacancies (V_{Al})-related complexes [59]. Besides, the created vacancies as point defects play a dominant role for stress relaxation [60]. During the stress relaxation, Al vacancies diffuse through $\text{Al}_x\text{Ga}_{1-x}\text{N}$ layer and form V_{Al} -related complexes, such as Al vacancy with nitrogen vacancy ($V_{\text{Al}} - V_{\text{N}}$) and Al vacancy with oxygen impurity in nitrogen site ($V_{\text{Al}} - \text{O}_{\text{N}}$) [61–63]. Al vacancies can enhance the strain relaxation rate by facilitating the initiation of atomic rearrangements in strained layers, which will also lead to a strain relaxation. Herein, Al atoms inhibit the electron mobility in $\text{Al}_x\text{Ga}_{1-x}\text{N}$ sample (S_3). This is attributed to the rise of the vacancies and point defect densities in thicker $\text{Al}_x\text{Ga}_{1-x}\text{N}$ sample. This proves the dominant role of Al atoms effect on electrical properties and on strain relaxation of $\text{Al}_x\text{Ga}_{1-x}\text{N}$ sample. Therefore, a strong correlation between them is established.

As shown above, it was demonstrated the close dependence between

physical $\text{Al}_x\text{Ga}_{1-x}\text{N}$ properties and the thickness effect. It is of paramount importance to analyze the evolution of sample thickness effect on nanomechanical properties of these investigated $\text{Al}_x\text{Ga}_{1-x}\text{N}$ thin films. In the following section, it is proposed to disclose the correlation between physical and nanomechanical features of $\text{Al}_x\text{Ga}_{1-x}\text{N}$ samples elaborated in the same gas-phase composition of TMAI and TMGa. It is worth to note that only S_1 , S_2 , and S_3 samples are analyzed. S_0 sample nanoindentation curves suffer from the substrate effect (as it is mentioned in the experimental details).

3.2. Analysis of nanoindentation results

Fig. 8a, b, and c display the loading-unloading curves associated with nanoindentation tests on $\text{Al}_x\text{Ga}_{1-x}\text{N}$ epilayers. Berkovich indenter was used to carry out the nanoindentation experiments at a maximal load of 4 mN with the loading rate of 0.15 mN/s. Nanoindentation curves show that the scattering is less pronounced along with the sample thickness. Fig. 8a displays a very wide dispersion in loading-unloading curves compared to the other curves. Nevertheless, in S_3 sample, the loading-unloading curves are less scattered and practically overlapped (Fig. 8c). This difference in loading-unloading responses is likely explained by the dissimilarity in contact surface underneath the indenter tip which depends on the $\text{Al}_x\text{Ga}_{1-x}\text{N}$ film thickness. In other words, an improvement in nanoindentation curves regularity is observed with film thickness increase. At the earlier stage of growth process, the surface coalescence is uncompleted and a high density of random pores appears (as seen in S_1 sample). This is resulting from the effect of the random SiN nano-mask deposited on sapphire substrate. Therefore, it results in a high scatter of nanomechanical film response. In contrast, for thicker $\text{Al}_x\text{Ga}_{1-x}\text{N}$ layer (S_3 sample), a smooth surface is observed once the 2D growth mode is achieved. By analyzing Fig. 8a, b, and c, it can be clearly seen that the indenter displacement depth is deeper in the S_1 sample than that in S_2 and S_3 samples. Hence, a low residual penetration depth after the unloading process is obtained with the increase of the film thickness. Thus, $\text{Al}_x\text{Ga}_{1-x}\text{N}$ film thickness thoroughly affects the plastic depth induced by nanoindentation. This is probably due to the hardening effect induced by the increase in the film thickness and by the decrease of the surface porosity. The plastic work W_p , given by the area inside loading-unloading curves, is calculated for the three $\text{Al}_x\text{Ga}_{1-x}\text{N}$ samples, at the maximal load of 4 mN. The value of plastic work is evaluated at $(94 \pm 17) \times 10^{-12} \text{ J}$, $(66 \pm 10) \times 10^{-12} \text{ J}$, and $(54 \pm 5) \times 10^{-12} \text{ J}$ for S_1 , S_2 and S_3 samples, respectively. These results reveal that the average plastic work decreases with increasing film thickness. This means that the material is losing its plastic ductility, when the surface of $\text{Al}_x\text{Ga}_{1-x}\text{N}$ film becomes denser. For all samples, the loading curves pop-in events have appeared as a plateau marking the initiation of plastic deformation, as displayed in Fig. 8a, b, and c. During the loading, when the critical value of shear stress in a small subsurface volume is reached, the homogeneous nucleation and emission of dislocation loops is activated and leads to the formation of the slip lines [64]. Multi-level positions of pop-in events are observed in all samples corresponding to multi critical indentation loads P_{cr} which represent the threshold of the plastic deformation by nanoindentation. The values of pop-in critical load and pop-in width are about $(2.6 \pm 0.9) \text{ mN}$, $(2.5 \pm 0.5) \text{ mN}$ and $(2.4 \pm 0.3) \text{ mN}$, and $(9 \pm 4) \text{ nm}$, $(8 \pm 2) \text{ nm}$ and $(7 \pm 2) \text{ nm}$ for S_1 , S_2 and S_3 samples, respectively. It is worth to note that the decrease of the average value of the pop-in critical load and pop-in width along with $\text{Al}_x\text{Ga}_{1-x}\text{N}$ layer thickness is attributed to the achievement of 2D growth mode and to the Al incorporation enhancement [57] conveyed by the increase of point defects [65], which increase the bond strength and the resistance to the formation of dislocations [18]. This is likely attributed to the noticed hardening raise as a function of $\text{Al}_x\text{Ga}_{1-x}\text{N}$ film thickness.

Fig. 9 shows the evolution of Young's modulus and hardness as a function of $\text{Al}_x\text{Ga}_{1-x}\text{N}$ film thickness. These results were averaged over all the nanoindentation experiments obtained for each sample.

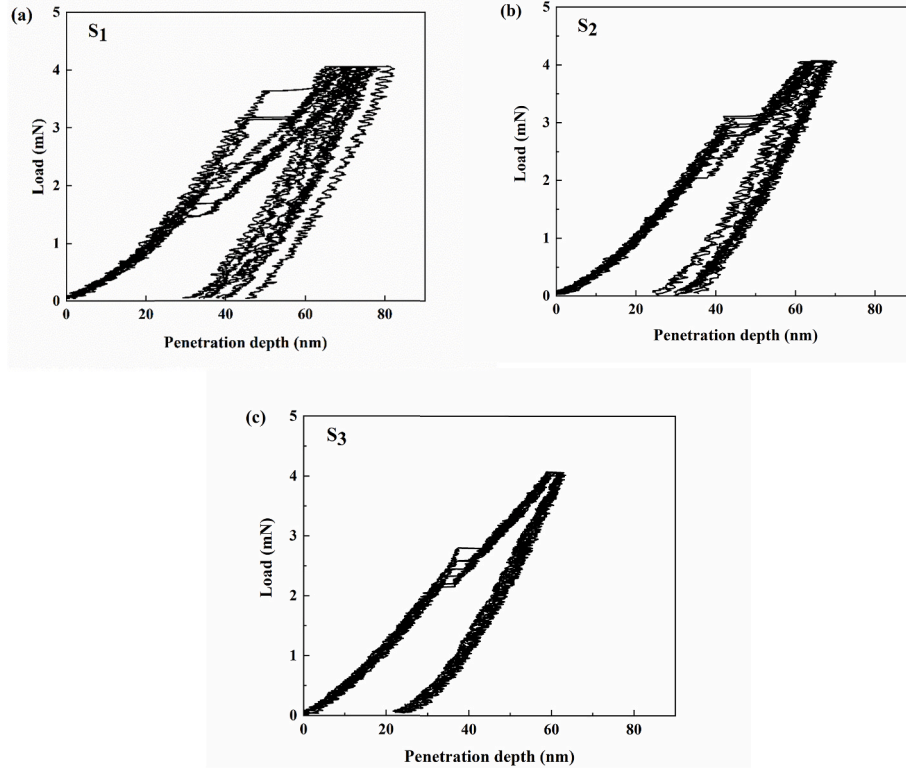


Fig. 8. Experimental loading-unloading curves versus the penetration depth of $\text{Al}_x\text{Ga}_{1-x}\text{N}$ samples elaborated at different film thickness; (a) S_1 , (b) S_2 and (c) S_3 .

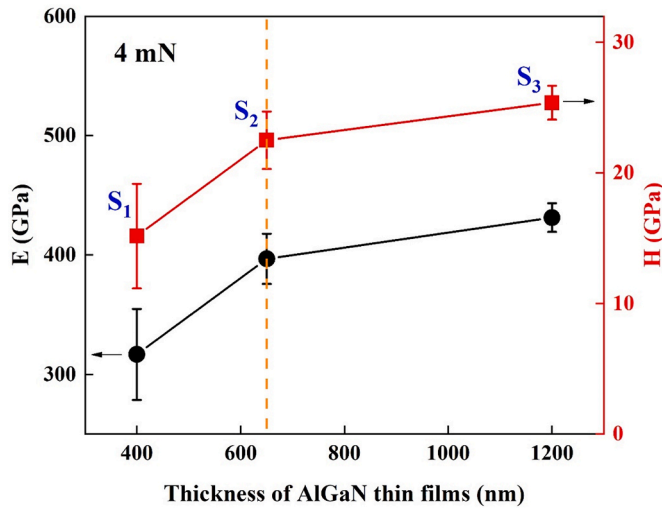


Fig. 9. Elastic modulus E and hardness H values versus sample thickness, measured at a maximum load of 4 mN and obtained for S_1 , S_2 and S_3 $\text{Al}_x\text{Ga}_{1-x}\text{N}$ thin films. Dashed line marks the transition from 3D to 2D growth mode.

Oliver–Pharr data analysis procedure [42] was used to determine nanomechanical properties of $\text{Al}_x\text{Ga}_{1-x}\text{N}$ thin films.

Hardness is defined as the maximum indentation load divided by the projected contact area of the indentation imprint.

$$H = \frac{P_{\max}}{A_c} \quad (4)$$

where, P_{\max} and A_c are the maximum load and the projected area, respectively.

The elastic modulus was obtained using the following relation:

$$\frac{1}{E_r} = \frac{1 - \nu^2}{E} + \frac{1 - \nu_i^2}{E_i} \quad (5)$$

where, (E, ν) and (E_i, ν_i) are the elastic modulus and Poisson coefficient of the film and the indenter, respectively. For diamond tip, the elastic modulus E_i and Poisson coefficient ν_i are 1141 GPa and 0.07, respectively.

The reduced elastic modulus E_r is expressed by:

$$E_r = \frac{1}{2\beta} \sqrt{\frac{\pi}{A_c}} S \quad (6)$$

where, S is the measured contact stiffness, β is a shape constant which is equal to 1.034 for a perfect Berkovich indenter.

At 4 mN, the hardness and the elastic modulus values of $\text{Al}_x\text{Ga}_{1-x}\text{N}$ films increase with high slope for the uncoalesced surface samples, then they increase with low slope for coalesced surfaces. In fact, at the first growth stage (3D growth mode), the rise of hardness and Young's modulus could be explained by the dwindle of pores density of the film surface along with the film thickness. Chen et al. [66] suggest that the hardness and the elastic modulus increase with decreasing porosity. However, as the film thickness continues to arise, the sample surface coalesces (2D growth mode) and Al incorporation increases which is conveyed by the point defects. As $\text{Al}_x\text{Ga}_{1-x}\text{N}$ is the formation of native defects and their complexes, such as Al vacancy complex [61,62], the introduced defects are likely the main reason for the enhancement of nanomechanical properties. We propose to provide more insights into the interpretation of nanomechanical behavior by elucidating the mechanisms that influence the nanomechanical properties of $\text{Al}_x\text{Ga}_{1-x}\text{N}$ samples. It is interesting to highlight that the nanomechanical properties are dictated by the biaxial stress magnitude, residual threading dislocations, point defects and their interactions with the generated dislocations produced underneath the indenter tip by plastic deformation over the nanoindentation test. Owing to the effect of SiN treatment, the residual dislocations produced during the growth process are highly

reduced, as long as moving away from the interface between substrate/ $\text{Al}_x\text{Ga}_{1-x}\text{N}$ layer. Then, the stress relaxation and the coalescence process of $\text{Al}_x\text{Ga}_{1-x}\text{N}$ layer are occurred promoting the Al vacancy creation [60]. On the other hand, MOCVD is the used $\text{Al}_x\text{Ga}_{1-x}\text{N}$ growth process at atmospheric pressure, then high parasitic reactions between the organometallic and ammonia with low Al atoms mobility (compared to Ga atoms) are also sources of high density of Al vacancy. These latter are associated with nitrogen vacancy and oxygen impurity in nitrogen site to form V_{Al} -related complexes. In addition, the impurities, e.g., carbon, silicon, oxygen, etc., that are introduced near the interface sapphire/ $\text{Al}_x\text{Ga}_{1-x}\text{N}$ layer are likely diffusing through the dislocation lines [57]. These point defects can act as obstacles to the dislocation motion, either individually or collectively in various types of clusters [67]. Thereafter, they pinned the motion of dislocations which require an exceed of external loading for carrying on their emission and resulting in an increase of the hardness of $\text{Al}_x\text{Ga}_{1-x}\text{N}$. Commonly, such phenomenon is known as the strengthening effect.

At atmospheric pressure, it was found that the Al incorporation in $\text{Al}_x\text{Ga}_{1-x}\text{N}$ increases to attain a saturation ratio around 7%, as displayed by SIMS curves in Fig. 4. It is expected that for an increase of the $\text{Al}_x\text{Ga}_{1-x}\text{N}$ thickness beyond 1200 nm, the hardness and Young's modulus are likely to remain around steady values [19,68].

However, in the case of using appropriate growth conditions permitting a high augmentation of Al composition, the kinetic of surface coalescence increases [17]. Thus, the porosity disappeared fast and it results in the growth of smooth layers starting with small thicknesses. In this case, the hardness increases with the Al composition and the Young's modulus roughly remains constant. As high Al composition are further incorporated into $\text{Al}_x\text{Ga}_{1-x}\text{N}$ coalesced surface, the concentration of Ga atoms is reduced and approaching the AlN layers. The resulting hardness H is lower than that obtained for GaN layer. Indeed, the expected evolution of the hardness has some limit after which the nanomechanical properties drop down, to uptake the hardness value of AlN [19,69]. Nevertheless, the Young's modulus is less sensitive to the increase of Al composition, it converges towards a constant value, as reported in literature [19,68].

The onset of the plastic deformation is attained when the volume underneath the indenter tip reaches the maximal shear stress. Thus, it is interesting to determine this nanomechanical property for $\text{Al}_x\text{Ga}_{1-x}\text{N}$ samples. It is expressed by the following equation:

$$\tau_{\max} = 0.31 \left(\frac{6P_{\text{cr}}E^2}{\pi^3 R^2} \right)^{1/3} \quad (7)$$

P_{cr} is the critical indentation load, R is the radius of the indenter tip and E is the Young's modulus.

The maximal shear stresses obtained together with the parameters characterizing the nanomechanical properties of $\text{Al}_x\text{Ga}_{1-x}\text{N}$ thin films are listed in Table 2. The average maximal shear stress increases with the increase of the $\text{Al}_x\text{Ga}_{1-x}\text{N}$ film thickness. This suggests the increase of the film stiffness. Besides, the increase of the Young's modulus E is correlated with the hardness H and the degree elastic recovery, as shown in Table 2. Moreover, the H/E ratio is an important factor which expresses the endurance capacity and dependent on the fracture toughness of the tested thin films. Indeed, the lower H/E ratio, the higher fracture toughness is. For the three $\text{Al}_x\text{Ga}_{1-x}\text{N}$ samples, the H/E ratio is almost similar and relatively low which likely indicates a certain enhancement level of resistance to fracture when high loading is applied. This

nanomechanical behavior can be associated to the SiN treatment used in this set of $\text{Al}_x\text{Ga}_{1-x}\text{N}$ layers, which initiates 3D growth mode, then buried the threading dislocations.

However, one may wonder about the nanomechanical resistance of these $\text{Al}_x\text{Ga}_{1-x}\text{N}$ layers whenever high loadings are applied. What is the ultimate loading that the $\text{Al}_x\text{Ga}_{1-x}\text{N}$ layer could undergo without the revelation of cracks and failure? The response to these questions is very critical for the reliability of UV LEDs manufacturing processes. Therefore, in this study high indentation loading was applied. Fig. 10 displays the nanoindentation imprints revealed by SEM images of $\text{Al}_x\text{Ga}_{1-x}\text{N}$ samples with an applied load of 200 mN. One can observe that no visible cracks are detected. These results prove the high plastic deformation capacity of the elaborated $\text{Al}_x\text{Ga}_{1-x}\text{N}$ layers, which make them suitable for hard imprints.

Fig. 10 a and b prove the effect of surface porosity on the imprints and thus on the resulting hardness. In addition, Fig. 10 c and d show the imprint size marked on the S_3 sample which is smaller than that obtained on the S_2 sample. This evidently supposes that the S_3 sample is harder than the S_2 sample. This qualitative observation is in good agreement with the hardness evolution given in Fig. 9.

Mainly, the compromise between the aptitude capacity of plastic deformation and the suitable hardness/stiffness ratio (as antagonist properties) is desired. Currently, NIL is the most cost-effective method used to fabricate patterned substrates. An appropriate resist is patterned by nanomechanical contact using a working stamp to replicate an inverted copy of it on the resist. The thermal NIL [70] and UV NIL [71] are generally the most practiced NIL techniques. However, in the recent years, a variety of new NIL methods have been proposed, such as simultaneous thermal and UV method (STU) [72], laser-assisted direct imprint (LADI) [73], soft UV-NIL [74], electrical field-assisted NIL [75] and reverse NIL [76], which aim to improve the nanostructures fabrication of large scale devices, 3D features, high throughput, high resolution, and free defects. In addition, while the development of nanoimprint lithography is ongoing, it is also important to deploy efforts in the investigation of appropriateness between the new lithography techniques and the nanomechanical properties of elaborated semiconductor devices. In this context, we postulate an approach that could open new perspectives for implementing direct nanoimprint technology for the fabrication of UV LEDs. This new technology is likely to promote for the next generation lithography approaches, which can produce on III-nitrides, 3D features using working hard stamp to replicate an inverse pattern image of this stamp directly on a suitable $\text{Al}_x\text{Ga}_{1-x}\text{N}$ layer without the usage of conventional NIL techniques. Moreover, it seems that a laser-assisted direct hard stamping is probably a more operative approach to assist the imprint operation by heating the target layer for imprints. This can reduce the stamping efforts and increasing the depth of the grooves depending on the design and resolution of patterns to imprint.

To sum up, it is observed that, on one hand the trends of physical properties, such as the refractive index and the electron mobility of $\text{Al}_x\text{Ga}_{1-x}\text{N}$ layers are similar (i.e., an increase then a decrease) as the film thickness increases; on the other hand, the probed nanomechanical properties exhibit an improvement along with the film thickness augmentation. However, the dislocation density is continuously decreasing and being the lowest for the harder sample (S_3). In addition, it was reported that the residual strains and the grown-in threading dislocations in $\text{Al}_x\text{Ga}_{1-x}\text{N}$ layers have only shallow effects on the hardness [19]. This arguing is solved by the induced strain relaxation with

Table 2
Nanomechanical properties of $\text{Al}_x\text{Ga}_{1-x}\text{N}$ thin films (S_1 , S_2 and S_3).

Samples	Young's modulus (GPa)	Hardness (GPa)	H/E ratio (–)	Plastic work (10^{-12} J)	Maximum shear stress (GPa)	Degree of elastic recovery (–)
S_1	316 ± 38	15 ± 4	0.05 ± 0.01	94 ± 17	14.5 ± 1.9	0.34 ± 0.06
S_2	403 ± 21	22 ± 2	0.055 ± 0.008	66 ± 10	16.6 ± 0.7	0.43 ± 0.04
S_3	425 ± 12	24 ± 1	0.057 ± 0.004	54 ± 5	17.4 ± 0.5	0.46 ± 0.03

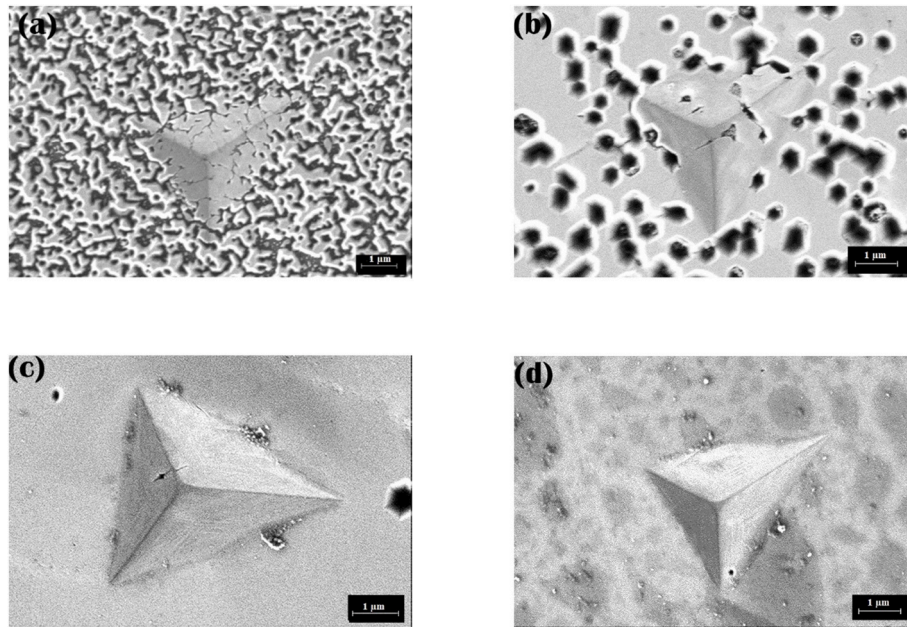


Fig. 10. SEM images obtained at a maximum load of 200 mN for different $\text{Al}_x\text{Ga}_{1-x}\text{N}$ thin films: (a) S_0 (b) S_1 , (c) S_2 and (d) S_3 .

the achievement of the surface coalescence which enhances the Al atoms incorporation conveyed with larger point defects. This likely establishes the good correlation between morphological, crystalline, optical, electrical and nanomechanical properties of $\text{Al}_x\text{Ga}_{1-x}\text{N}$ samples along with film thickness increase.

In order to highlight the Al atoms incorporation role on nanomechanical properties of $\text{Al}_x\text{Ga}_{1-x}\text{N}$ sample, a comparative study between $\text{Al}_x\text{Ga}_{1-x}\text{N}$ layer (S_3) and GaN of 1200 nm thickness is carried out. Furthermore, we attempt to establish a correlation between physical and nanomechanical properties for both $\text{Al}_x\text{Ga}_{1-x}\text{N}$ and GaN samples, giving that they were grown in the same growth conditions. Fig. 11 shows all nanoindentation tests that were performed at room temperature and atmospheric pressure, where the applied maximum load is about 10 mN with a loading rate of 0.15 mN/s. Firstly, it appears that the loading-unloading curves of GaN films deviated toward the right side corresponding to the high penetration depth compared to $\text{Al}_x\text{Ga}_{1-x}\text{N}$ curves.

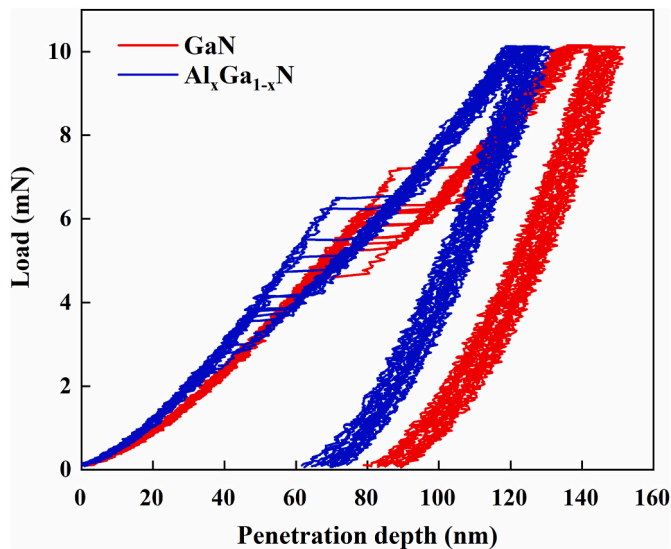


Fig. 11. Loading-unloading curves of GaN and $\text{Al}_x\text{Ga}_{1-x}\text{N}$ epilayers grown at the same growth conditions, with 10 mN as a maximum load and loading rate of 0.15 mN/s.

One can assume that the $\text{Al}_x\text{Ga}_{1-x}\text{N}$ film is harder than the GaN layer. Indeed, the hardness is about (20 ± 1) GPa and (15 ± 1) GPa, and Young's modulus is about (360 ± 8) GPa and (330 ± 6) GPa for $\text{Al}_x\text{Ga}_{1-x}\text{N}$ and GaN films, respectively.

Furthermore, the loading-unloading curves are almost overlapped, as can be seen for each sample. This can assume that the GaN and $\text{Al}_x\text{Ga}_{1-x}\text{N}$ samples show smooth surface, while the 2D growth mode was achieved. In addition, it can be clearly seen the presence of multiple pop-in events observed during loading process in both films. Besides, the scatter of the pop-in loading level is observed for both samples. In other words, the onset of plastic deformation depends on the indentation location and depth. This is ascribed to the non-homogeneous distribution of dislocations and point defects in samples. It is worth to note that SiN treatment of sapphire substrate along with a fraction of H_2 carrier gas, used in the growth process, play an important role in the formation and the distribution of the grown-in threading dislocations in the elaborated samples, as reported in Ref. [49]. Consequently, 7% of Al incorporation in S_3 sample contributes to increase the hardness and Young's modulus of $\text{Al}_x\text{Ga}_{1-x}\text{N}$ film of about 33% and 9%, respectively, compared to that found for GaN film. This corroborates the fact that the Al incorporation has a noticeable effect on hardness rather than on the Young's modulus, as it was speculated previously.

The pop-in width values are (12.9 ± 5.3) nm and (19.1 ± 2.5) nm for $\text{Al}_x\text{Ga}_{1-x}\text{N}$ and GaN samples, respectively. The pop-in critical load values of $\text{Al}_x\text{Ga}_{1-x}\text{N}$ and GaN samples are about (4.4 ± 1.1) mN and (5.8 ± 0.6) mN, respectively. Comparable findings were reported in the literature [22,77]. The pop-in critical load and pop-in width are lower in $\text{Al}_x\text{Ga}_{1-x}\text{N}$ layer than in GaN film. This behavior is observed for MgO samples which demonstrated that the lower pop-in loads and widths are decreased with increasing dislocation densities [25]. Thereafter, the lower value of the maximal shear stress is likewise obtained for $\text{Al}_x\text{Ga}_{1-x}\text{N}$ sample. It is about (18.8 ± 0.6) GPa and (19.5 ± 0.6) GPa for $\text{Al}_x\text{Ga}_{1-x}\text{N}$ and GaN films, respectively. The observed difference in the quantitative findings is attributed to the increase of the dislocation density (see, Fig. 3), the Al incorporation and the introduction of point defects into $\text{Al}_x\text{Ga}_{1-x}\text{N}$ layer.

The creep behavior of a material is a nanomechanical phenomenon which is observed when the plastic deformation occurs as function of the time for an applied constant load. For a dwell time of 30 s at a maximum force of 10 mN, the indenter continues to penetrate $\text{Al}_x\text{Ga}_{1-x}\text{N}$ and GaN

samples. The values of indenter depth during the creep were about (4.9 ± 1.5) nm and (9.9 ± 1.5) nm for $\text{Al}_x\text{Ga}_{1-x}\text{N}$ and GaN films, respectively. Thus, the lower penetration depth is obtained for the $\text{Al}_x\text{Ga}_{1-x}\text{N}$ film. Nanomechanical features are highly sensitive to the Al incorporation and point defects into $\text{Al}_x\text{Ga}_{1-x}\text{N}$ sample leading to the reduction of the pop-in critical load, the maximal shear stress and the creep depth compared to GaN film. However, the physical properties of $\text{Al}_x\text{Ga}_{1-x}\text{N}$ such as refractive index and electron mobility were degraded in comparison with GaN film. This establishes the good correlation between physical and nanomechanical properties of $\text{Al}_x\text{Ga}_{1-x}\text{N}$ and GaN samples.

4. Conclusion

In this work, film thickness effects on physical and nanomechanical properties of specific undoped $\text{Al}_x\text{Ga}_{1-x}\text{N}$ layers that were elaborated using MOCVD technique in the same gas phase composition of TMAI and TMGa were investigated. Two growth stages were distinguished owing to the deposition of random SiN nano-mask, which considerably reduces the mismatch between the sapphire substrate/ $\text{Al}_x\text{Ga}_{1-x}\text{N}$ layer; therefore the threading dislocations emerging at the layer surface were hindered. At the first growth stage, it was shown that the physical and nanomechanical properties were essentially dictated by the high surface porosity, low Al incorporation and continuous decrease of threading dislocations. Then, as long as the film gets thicker, the 2D growth mode is established and revealed by the surface coalescence of $\text{Al}_x\text{Ga}_{1-x}\text{N}$ film. At this step, the Al composition is increasing to attain a saturation value around 7% conveyed by point defects resulting in the stress relaxation and less effects of the grown-in threading dislocations on the nanomechanical properties. These point defects interact with the nucleated dislocations underneath the indenter tip, by pinning them and impeding their propagation. Consequently, it results in an increase of the $\text{Al}_x\text{Ga}_{1-x}\text{N}$ hardness and weak effect on the Young's modulus. However, SEM images display free cracks in the nanoimprints obtained using high loading force. This demonstrates that the elaborated $\text{Al}_x\text{Ga}_{1-x}\text{N}$ layers are featured by both high plastic deformation (ductility) and endurance (fracture toughness) capacities, which make them suitable for the implementation of prospective approach for the next generation lithography techniques. The compromise between the high $\text{Al}_x\text{Ga}_{1-x}\text{N}$ ductility and its appropriate nanomechanical properties, open the perspectives for a new NIL method based on direct nanoimprint via laser assisted nanomechanical contact using working hard stamp. This can contribute to throughput and low-cost technology for the fabrication of patterned UV LEDs to improve their light output power.

CRediT authorship contribution statement

N. Boughrara: Writing – review & editing, Writing – original draft, Validation, Methodology, Investigation. **Z. Benzarti:** Writing – review & editing, Writing – original draft, Visualization, Validation, Supervision, Methodology, Investigation, Conceptualization. **A. Khalfallah:** Writing – review & editing, Writing – original draft, Validation, Methodology, Investigation, Conceptualization. **J.C. Oliveira:** Validation, Resources, Methodology, Investigation. **M. Evaristo:** Resources, Methodology. **A. Cavaleiro:** Resources, Methodology.

Declaration of competing interest

The authors declare that they have no known competing financial interests or personal relationships that could have appeared to influence the work reported in this paper.

Data availability

Data will be made available on request.

References

- [1] J.S. Park, Z.J. Reitmeier, D. Fothergill, X. Zhang, J.F. Muth, R.F. Davis, Growth and fabrication of AlGaIn-based ultraviolet light emitting diodes on 6H-SiC(0 0 1) substrates and the effect of carrier-blocking layers on their emission characteristics, *Mater. Sci. Eng., B* 127 (2006) 169–179, <https://doi.org/10.1016/j.mseb.2005.10.019>.
- [2] H.Y. Ryu, I.G. Choi, H.S. Choi, J.I. Shim, Investigation of light extraction efficiency in AlGaIn deep-ultraviolet light-emitting diodes, *Appl. Phys. Express* 6 (2013), <https://doi.org/10.7567/APEX.6.062101>.
- [3] Z. Benzarti, T. Sekrafi, Z. Bougrioua, A. Khalfallah, B. El Jani, Effect of SiN treatment on optical properties of InxGa1-xN/GaN MQW blue LEDs, *J. Electron. Mater.* 46 (2017) 4312–4320, <https://doi.org/10.1007/s11664-017-5383-2>.
- [4] H. Yoshida, M. Kuwabara, Y. Yamashita, Y. Takagi, K. Uchiyama, H. Kan, AlGaIn-based laser diodes for the short-wavelength ultraviolet region, *New J. Phys.* 11 (2009) 3, <https://doi.org/10.1088/1367-2630/11/12/125013>.
- [5] H. Yoshida, Y. Yamashita, M. Kuwabara, H. Kan, A 342-nm ultraviolet AlGaIn multiple-quantum-well laser diode, *Nat. Photonics* 2 (2008) 551–554, <https://doi.org/10.1038/nphoton.2008.135>.
- [6] S. Nakamura, M. Senoh, S. Nagahama, N. Iwasa, T. Yamada, T. Matsushita, H. Kiyoku, Y. Sugimoto, InGaIn-based multi-quantum-well-structure laser diodes, *Jpn. J. Appl. Phys.* 35 (1996), <https://doi.org/10.1143/JJAP.35.L74>.
- [7] O. Ambacher, M. Eickhoff, A. Link, M. Hermann, M. Stutzmann, F. Bernardini, V. Fiorentini, Y. Smorchkova, J. Speck, U. Mishra, W. Schaff, V. Tilak, L. F. Eastman, Electronics and sensors based on pyroelectric AlGaIn/GaN heterostructures: Part A: polarization and pyroelectronics, *Phys. Status Solidi C Conf.* (2003) 1878–1907, <https://doi.org/10.1002/pssc.200303138>, 0.
- [8] T.K. Ko, S.J. Chang, Y.K. Su, M.L. Lee, C.S. Chang, Y.C. Lin, S.C. Shei, J.K. Sheu, W. S. Chen, C.F. Shen, AlGaIn-GaN Schottky-barrier photodetectors with LT GaN cap layers, *J. Cryst. Growth* 283 (2005) 68–71, <https://doi.org/10.1016/j.jcrysgro.2005.05.067>.
- [9] M.-L. Lee, T.S. Mue, F.W. Huang, J.H. Yang, J.K. Sheu, High-performance GaN metal-insulator-semiconductor ultraviolet photodetectors using gallium oxide as gate layer, *Opt Express* 19 (2011), 12658, <https://doi.org/10.1364/oe.19.012658>.
- [10] M. Kneissl, T.Y. Seong, J. Han, H. Amano, The emergence and prospects of deep-ultraviolet light-emitting diode technologies, *Nat. Photonics* 13 (2019) 233–244, <https://doi.org/10.1038/s41566-019-0359-9>.
- [11] P. Makaram, J. Joh, J.A. Del Alamo, T. Palacios, C.V. Thompson, Evolution of structural defects associated with electrical degradation in AlGaIn/GaN high electron mobility transistors, *Appl. Phys. Lett.* 96 (2010), <https://doi.org/10.1063/1.3446869>.
- [12] Z. Benzarti, M. Khelifi, A. Khalfallah, B. El Jani, Assessment of refractive index changes by spectral reflectance in the first stages of AlxGa1-xN layer growth using SiN treatment, *J. Mater. Sci. Mater. Electron.* 27 (2016) 6336–6346, <https://doi.org/10.1007/s10854-016-4568-4>.
- [13] H. Yang, X. Zhang, S. Wang, M. Zhu, Y. Cui, Quantitative study for surface properties of AlGaIn epi-layers by ARXPS, *EPJ Appl. Phys.* 72 (2015), 20301, <https://doi.org/10.1051/epjap/2015150418>.
- [14] S.S. Pasayat, N. Hatui, W. Li, C. Gupta, S. Nakamura, S.P. Denbars, S. Keller, U. K. Mishra, Method of growing elastically relaxed crack-free AlGaIn on GaN as substrates for ultra-wide bandgap devices using porous GaN, *Appl. Phys. Lett.* 117 (2020), 62102, <https://doi.org/10.1063/5.0017948>.
- [15] S. Lazarev, M. Barchuk, S. Bauer, K. Forghani, V. Holý, F. Scholz, T. Baumbach, Study of threading dislocation density reduction in AlGaIn epilayers by Monte Carlo simulation of high-resolution reciprocal-space maps of a two-layer system, *J. Appl. Crystallogr.* 46 (2013) 120–127, <https://doi.org/10.1107/S0021889812043051>.
- [16] D.G. Zhao, Z.S. Liu, J.J. Zhu, S.M. Zhang, D.S. Jiang, H. Yang, J.W. Liang, X.Y. Li, H.M. Gong, Effect of Al incorporation on the AlGaIn growth by metalorganic chemical vapor deposition, *Appl. Surf. Sci.* 253 (2006) 2452–2455, <https://doi.org/10.1016/j.apsusc.2006.04.062>.
- [17] Z. Benzarti, I. Halidou, A. Touré, B. El Jani, Al, Incorporation at all growth stages of AlxGa1-xN epilayers using SiN treatment, *J. Electron. Mater.* 45 (2016) 872–880, <https://doi.org/10.1007/s11664-015-4240-4>.
- [18] F.J. Xu, B. Shen, M.J. Wang, J. Xu, L. Lu, Z.L. Miao, Z.J. Yang, Z.X. Qin, G.Y. Zhang, B. Lin, S.L. Bai, Mechanical properties of Alx Ga1-x N films with high Al composition grown on AlN/sapphire templates, *Appl. Phys. Lett.* 91 (2007), <https://doi.org/10.1063/1.2735551>.
- [19] Y. Tokumoto, H. Taneichi, Y. Ohno, K. Kutsukake, H. Miyake, K. Hiramatsu, I. Yonenaga, Nanoindentation hardness and elastic modulus of AlGaIn alloys, *Pacific Rim Conf. Lasers Electro-Optics, CLEO - Tech. Dig.* (2013), <https://doi.org/10.1109/CLEOPR.2013.6600379>.
- [20] J.E. Bradby, S.O. Kucheyev, J.S. Williams, J. Wong-Leung, M.V. Swain, P. Munroe, G. Li, M.R. Phillips, Indentation-induced damage in GaN epilayers, *Appl. Phys. Lett.* 80 (2002) 383–385, <https://doi.org/10.1063/1.1436280>.
- [21] S.R. Jian, Mechanical deformation induced in Si and GaN under Berkovich nanoindentation, *Nanoscale Res. Lett.* 3 (2008) 6–13, <https://doi.org/10.1007/s11671-007-9106-0>.
- [22] S.O. Kucheyev, J.E. Bradby, J.S. Williams, C. Jagadish, M. Toth, M.R. Phillips, M. V. Swain, Nanoindentation of epitaxial GaN films, *Appl. Phys. Lett.* 77 (2000) 3373–3375, <https://doi.org/10.1063/1.1328047>.
- [23] Z. Benzarti, T. Sekrafi, A. Khalfallah, Z. Bougrioua, D. Vignaud, M. Evaristo, A. Cavaleiro, Growth temperature effect on physical and mechanical properties of nitrogen rich InN epilayers, *J. Alloys Compd.* 885 (2021), 160951, <https://doi.org/10.1016/j.jallcom.2021.160951>.

- [24] T.H. Ahn, C.S. Oh, K. Lee, E.P. George, H.N. Han, Relationship between yield point phenomena and the nanoindentation pop-in behavior of steel, *J. Mater. Res.* 27 (2012) 39–44, <https://doi.org/10.1557/jmr.2011.208>.
- [25] A. Montagne, V. Audurier, C. Tromas, Influence of pre-existing dislocations on the pop-in phenomenon during nanoindentation in MgO, *Acta Mater.* 61 (2013) 4778–4786, <https://doi.org/10.1016/j.actamat.2013.05.004>.
- [26] X.Q. Yan, X.M. Huang, S. Uda, M.W. Chen, Effect of heavy boron doping on pressure-induced phase transitions in single-crystal silicon, *Appl. Phys. Lett.* 87 (2005) 1–3, <https://doi.org/10.1063/1.2120920>.
- [27] J.E. Bradby, J.S. Williams, J. Wong-Leung, M.V. Swain, P. Munroe, Mechanical deformation of InP and GaAs by spherical indentation, *Appl. Phys. Lett.* 78 (2001) 3235–3237, <https://doi.org/10.1063/1.1372207>.
- [28] S. Kamiyama, M. Iwaya, N. Hayashi, T. Takeuchi, H. Amano, I. Akasaki, S. Watanabe, Y. Kaneko, N. Yamada, Low-temperature-deposited AlGaIn interlayer for improvement of AlGaIn/GaN heterostructure, *J. Cryst. Growth* 223 (2001) 83–91, [https://doi.org/10.1016/S0022-0248\(00\)01017-4](https://doi.org/10.1016/S0022-0248(00)01017-4).
- [29] C.F. Shih, N.C. Chen, S.Y. Lin, K.S. Liu, AlGaIn films grown on (0001) sapphire by a two-step method, *Appl. Phys. Lett.* 86 (2005) 1–3, <https://doi.org/10.1063/1.1931058>.
- [30] U. Zeimer, V. Kueller, A. Knauer, A. Mogilatenko, M. Meyers, M. Kneissl, High quality AlGaIn grown on ELO AlN/sapphire templates, *J. Cryst. Growth* 377 (2013) 32–36, <https://doi.org/10.1016/j.jcrysgro.2013.04.041>.
- [31] K. Forghani, M. Gharavipour, M. Klein, F. Scholz, O. Klein, U. Kaiser, M. Feneberg, B. Neuschl, K. Thonke, In-situ deposited SiNx nanomask for crystal quality improvement in AlGaIn, *Phys. Status Solidi Curr. Top. Solid State Phys.* 8 (2011) 2063–2065, <https://doi.org/10.1002/pssc.201001074>.
- [32] Z. Benzarti, M. Khelifi, I. Halidou, B. El Jani, Study of surface and interface roughness of GaN-based films using spectral reflectance measurements, *J. Electron. Mater.* 44 (2015) 3243–3252, <https://doi.org/10.1007/s11664-015-3855-9>.
- [33] S.Y. Chou, P.R. Krauss, P.J. Renstrom, Imprint of sub-25 nm vias and trenches in polymers, *Appl. Phys. Lett.* 67 (1995) 3114, <https://doi.org/10.1063/1.114851>.
- [34] C.C. Kao, Y.K. Su, C.L. Lin, J.J. Chen, The aspect ratio effects on the performances of GaN-based light-emitting diodes with nanopatterned sapphire substrates, *Appl. Phys. Lett.* 97 (2010), <https://doi.org/10.1063/1.3463471>.
- [35] K.-C. Shen, D.-S. Wu, C.-C. Shen, S.-L. Ou, R.-H. Horng, Surface modification on wet-etched patterned sapphire substrates using plasma treatments for improved GaN crystal quality and LED performance, *J. Electrochem. Soc.* 158 (2011) H988, <https://doi.org/10.1149/1.3616019>.
- [36] C.H. Kuo, H.C. Feng, C.W. Kuo, C.M. Chen, L.W. Wu, G.C. Chi, Nitride-based near-ultraviolet light emitting diodes with meshed p-GaN, *Appl. Phys. Lett.* 90 (2007), <https://doi.org/10.1063/1.2720347>.
- [37] T. Fujii, Y. Gao, R. Sharma, E.L. Hu, S.P. DenBaars, S. Nakamura, Increase in the extraction efficiency of GaN-based light-emitting diodes via surface roughening, *Appl. Phys. Lett.* 84 (2004) 855–857, <https://doi.org/10.1063/1.1645992>.
- [38] W. Zhou, G. Min, Z. Song, J. Zhang, Y. Liu, J. Zhang, Enhanced efficiency of light emitting diodes with a nano-patterned gallium nitride surface realized by soft UV nanoimprint lithography, *Nanotechnology* 21 (2010), <https://doi.org/10.1088/0957-4484/21/20/205304>.
- [39] C. Hyun Kyong, J. Junho, C. Jeong-Hyeon, C. Jaewan, K. Jongwook, L. Jeong Soo, L. Beomseok, C. Young Ho, L. Ki-Dong, K.S. Hoon, Light extraction enhancement from nano-imprinted photonic crystal GaN-based blue light-emitting diodes, *Opt Express* 14 (2006) 8654–8660.
- [40] Z. Benzarti, I. Halidou, T. Boufaden, B. El Jani, S. Juillaguet, M. Ramonda, Effect of SiN treatment on GaN epilayer quality, *Phys. Status Solidi Appl. Res.* 201 (2004) 502–508, <https://doi.org/10.1002/pssa.200306733>.
- [41] I. Halidou, Z. Benzarti, T. Boufaden, B. El Jani, S. Juillaguet, M. Ramonda, Influence of silane flow on MOVPE grown GaN on sapphire substrate by an in situ SiN treatment, *Mater. Sci. Eng. B Solid-State Mater. Adv. Technol.* 110 (2004) 251–255, <https://doi.org/10.1016/j.mseb.2004.02.002>.
- [42] W.C. Oliver, G.M. Pharr, An improved technique for determining hardness and elastic modulus using load and displacement sensing indentation experiments, *J. Mater. Res.* 7 (1992) 1564–1583, <https://doi.org/10.1557/jmr.1992.1564>.
- [43] I. Halidou, Z. Benzarti, H. Fitouri, W. Fathallah, B. El Jani, GaN property evolution at all stages of MOVPE Si/N treatment growth, *Phys. Status Solidi Curr. Top. Solid State Phys.* 4 (2007) 129–132, <https://doi.org/10.1002/pssc.200673532>.
- [44] J.E. Ayers, The measurement of threading dislocation densities in semiconductor crystals by X-ray diffraction, *J. Cryst. Growth* 135 (1994) 71–77, [https://doi.org/10.1016/0022-0248\(94\)90727-7](https://doi.org/10.1016/0022-0248(94)90727-7).
- [45] M.A. Moram, M.E. Vickers, X-ray diffraction of III-nitrides, *Rep. Prog. Phys.* 72 (2009), 36502, <https://doi.org/10.1088/0034-4885/72/3/036502>.
- [46] D.M. Follstaedt, S.R. Lee, A.A. Allerman, J.A. Floro, Strain relaxation in AlGaIn multilayer structures by threading dislocations, *J. Appl. Phys.* 105 (2009), 83507, <https://doi.org/10.1063/1.3087515>.
- [47] A. Sangghaleh, E. Pan, X. Han, Near-interface charged dislocations in AlGaIn/GaN bilayer heterostructures, *Appl. Phys. Lett.* 105 (2014) 2, <https://doi.org/10.1063/1.4895511>.
- [48] W. Li, S. Xu, Y. Zhang, R. Peng, J. Du, Y. Zhao, X. Fan, J. Zhang, H. Tao, X. Wang, Y. Hao, GaN quality evolution according to carrier gas for the nucleation layer and buffer layer, *Opt. Mater. Express* 9 (2019) 1945, <https://doi.org/10.1364/ome.9.001945>.
- [49] N. Boughrara, Z. Benzarti, A. Khalfallah, M. Evaristo, A. Cavaleiro, Comparative study on the nanomechanical behavior and physical properties influenced by the epitaxial growth mechanisms of GaN thin films, *Appl. Surf. Sci.* 579 (2022) 8, <https://doi.org/10.1016/j.apsusc.2021.151888>.
- [50] M. Tchounkeu, O. Briot, B. Gil, J.P. Alexis, R.L. Aulombard, Optical properties of GaN epilayers on sapphire, *J. Appl. Phys.* 80 (1996) 5352–5360, <https://doi.org/10.1063/1.363475>.
- [51] J. Han, J.J. Figiel, M.H. Crawford, M.A. Banas, M.E. Bartram, R.M. Biefeld, Y. K. Song, A.V. Nurmikko, OMVPE growth and gas-phase reactions of AlGaIn for UV emitters, *J. Cryst. Growth* 195 (1998) 291–296, [https://doi.org/10.1016/S0022-0248\(98\)00675-7](https://doi.org/10.1016/S0022-0248(98)00675-7).
- [52] D.G. Zhao, D.S. Jiang, J.J. Zhu, Z.S. Liu, S.M. Zhang, H. Yang, U. Jahn, K.H. Ploog, Al composition variations in AlGaIn films grown on low-temperature GaN buffer layer by metalorganic chemical vapor deposition, *J. Cryst. Growth* 310 (2008) 5266–5269, <https://doi.org/10.1016/j.jcrysgro.2008.09.167>.
- [53] H.Y. Lin, Y.F. Chen, T.Y. Lin, C.F. Shih, K.S. Liu, N.C. Chen, Direct evidence of compositional pulling effect in AlGaIn 1-xN epilayers, *J. Cryst. Growth* 290 (2006) 225–228, <https://doi.org/10.1016/j.jcrysgro.2006.01.021>.
- [54] R.F. Davis III-V, Nitrides for electronic and optoelectronic applications, *Proc. IEEE* 79 (1991) 702–712, <https://doi.org/10.1109/5.90133>.
- [55] J.M. Bethoux, P. Vennéguès, F. Natali, E. Feltn, O. Tottreau, G. Nataf, P. De Mierry, F. Sémont, Growth of high quality crack-free AlGaIn films on GaN templates using plastic relaxation through buried cracks, *J. Appl. Phys.* 94 (2003) 6499–6507, <https://doi.org/10.1063/1.1622993>.
- [56] M. Pérez Caro, A.C. Mejía, A.G. Rodríguez, H. Navarro-Contreras, M.A. Vidal, In situ measurements of the critical thickness for strain relaxation in β -GaN/MgO structures, *J. Cryst. Growth* 311 (2009) 1302–1305, <https://doi.org/10.1016/j.jcrysgro.2008.12.027>.
- [57] A.F. Vyatkin, The role of point defects in strain relaxation in epitaxially grown SiGe structures, *Thin Solid Films* 508 (2006) 90–95, <https://doi.org/10.1016/j.tsf.2005.08.405>.
- [58] N. Antoine-Vincent, F. Natali, M. Mihailovic, A. Vasson, J. Leymarie, P. Disseix, D. Byrne, F. Sémont, J. Massies, Determination of the refractive indices of AlN, GaN, and AlGaIn-xN grown on (111)Si substrates, *J. Appl. Phys.* 93 (2003) 5222–5226, <https://doi.org/10.1063/1.1563293>.
- [59] D.C. Look, R.J. Molnar, Degenerate layer at GaN/sapphire interface: influence on Hall-effect measurements, *Appl. Phys. Lett.* 70 (1997) 3377–3379, <https://doi.org/10.1063/1.119176>.
- [60] W. Gruber, S. Chakravarty, C. Baehtz, W. Leitenberger, M. Bruns, A. Kobler, K. Kübel, H. Schmidt, Strain relaxation and vacancy creation in thin platinum films, *Phys. Rev. Lett.* 107 (2011), <https://doi.org/10.1103/PhysRevLett.107.265501>.
- [61] S.F. Chichibu, A. Uedono, K. Kojima, H. Ikeda, K. Fujito, S. Takashima, M. Edo, K. Ueno, S. Ishibashi, The origins and properties of intrinsic nonradiative recombination centers in wide bandgap GaN and AlGaIn, *J. Appl. Phys.* 123 (2018), <https://doi.org/10.1063/1.5012994>.
- [62] C.W. Ahn, S. Park, E.K. Kim, Effect of oxygen on defect states of Al_{0.4}Ga_{0.6}N layers grown by hydride vapor phase epitaxy, *J. Mater. Res. Technol.* 17 (2022) 1485–1490, <https://doi.org/10.1016/j.jmrt.2022.01.101>.
- [63] S. Ichikawa, M. Funato, Y. Kawakami, Dominant nonradiative recombination paths and their activation processes in AlGaIn-xN-related materials, *Phys. Rev. Appl.* 10 (2018), <https://doi.org/10.1103/PhysRevApplied.10.064027>.
- [64] C. Tromas, Y. Gaillard, J. Woignard, Nucleation of dislocations during nanoindentation in MgO, *Philos. Mag. A* 86 (2006) 5595–5606, <https://doi.org/10.1080/14786430600690499>.
- [65] T. Ohmura, M. Wakeda, Pop-in phenomenon as a fundamental plasticity probed by nanoindentation technique, *Materials* 14 (2021) 2021, <https://doi.org/10.3390/ma14081879>.
- [66] X. Chen, Y. Xiang, J.J. Vlassak, Novel technique for measuring the mechanical properties of porous materials by nanoindentation, *J. Mater. Res.* 21 (2006) 715–724, <https://doi.org/10.1557/jmr.2006.0088>.
- [67] A.V. Shul'diner, V.A. Zakrevskii, The mechanism of interaction of dislocations with point defects in ionic crystals, *J. Phys. Condens. Matter* 14 (2002) 9555–9562, <https://doi.org/10.1088/0953-8984/14/41/311>.
- [68] D. Cáceres, I. Vergara, R. González, E. Monroy, F. Calle, E. Muñoz, F. Omnes, Nanoindentation on AlGaIn thin films, *J. Appl. Phys.* 86 (1999) 6773–6778, <https://doi.org/10.1063/1.371726>.
- [69] S.R. Jian, J.Y. Juang, Indentation-induced mechanical deformation behaviors of AlN thin films deposited on c-plane sapphire, *J. Nanomater.* 2012 (2012), <https://doi.org/10.1155/2012/914184>.
- [70] C. Con, J. Zhang, Z. Jahed, T.Y. Tsui, M. Yavuz, B. Cui, Thermal nanoimprint lithography using fluoropolymer mold, *Microelectron. Eng.* 98 (2012) 246–249, <https://doi.org/10.1016/j.mee.2012.07.007>.
- [71] K. Mohamed, Nanoimprint lithography for nanomanufacturing, *Compr. Nanosci. Nanotechnol.* 1–5 (2019) 357–386, <https://doi.org/10.1016/B978-0-12-803581-8.10508-9>.
- [72] F. Brunetti, S. Harrer, G. Scarpa, P. Lugli, M. Kubenz, C. Schuster, F. Reuther, Pattern transfer process using innovative polymers in combined thermal and UV nanoimprint lithography (TUV-NIL), *Mater. Res. Soc. Symp. Proc.* 1002 (2007) 1–6, <https://doi.org/10.1557/proc-1002-n03-01>.
- [73] S.Y. Chou, C. Keimel, J. Gu, Ultrafast and direct imprint of nanostructures in silicon, *Nature* 417 (2002) 835–837, <https://doi.org/10.1038/nature00792>.
- [74] M.J. Haslinger, T. Mitteramskogler, S. Kopp, H. Leichtfried, M. Messerschmidt, M. W. Thesen, M. Mühlberger, Development of a soft UV-NIL step&repeat and lift-off process chain for high speed metal nanomesh fabrication, *Nanotechnology* 31 (2020), <https://doi.org/10.1088/1361-6528/ab9130>.

- [75] C. Wang, J. Shao, H. Tian, X. Li, Y. Ding, B.Q. Li, Step-controllable electric-field-assisted nanoimprint lithography for uneven large-area substrates, *ACS Nano* 10 (2016) 4354–4363, <https://doi.org/10.1021/acs.nano.5b08032>.
- [76] N. Kehagias, V. Reboud, G. Chansin, M. Zelsmann, C. Jeppesen, F. Reuther, C. Schuster, M. Kubenz, G. Gruetzner, C.M. Sotomayor Torres, Submicron three-dimensional structures fabricated by reverse contact UV nanoimprint lithography, *J. Vac. Sci. Technol. B Microelectron. Nanom. Struct.* 24 (2006) 3002, <https://doi.org/10.1116/1.2388962>.
- [77] C.Y. Huang, P.J. Hsieh, I.C. Chen, W.C. Ke, P.F. Yang, S.R. Jian, Nanoindentation of Mg-doped AlGa_N thin films, *J. Alloys Compd.* 593 (2014) 220–223, <https://doi.org/10.1016/j.jallcom.2013.12.222>.